ADVANCED ELECTRONIC MATERIALS Open Access
www.advelectronicmat.de

Perovskite Thin Single Crystal for a High Performance and Long Endurance Memristor

Ismael Fernandez-Guillen, Clara A. Aranda, Pablo F. Betancur, Marta Vallés-Pelarda, Cristina Momblona, Teresa S. Ripolles, Rafael Abargues, and Pablo P. Boix**

Metal halide perovskites (MHPs) exhibit electronic and ionic characteristics suitable for memristors. However, polycrystalline thin film perovskite memristors often suffer from reliability issues due to grain boundaries, while bulk single-crystal perovskite memristors struggle to achieve high LRS/HRS ratios. In this study, a single crystal memristive device utilizing a wide bandgap perovskite is introduced, $MAPbBr_3$, in a high surface/thickness configuration. This thin single crystal overcomes these challenges, exhibiting a remarkable LRS/HRS ratio of up to 50 and endurance of 10^3 cycles, representing one of the highest reported values to date. This exceptional stability enables to analyze the electroforming process and LRS through impedance spectroscopy, providing insights into the underlying operational mechanism. As far as it is known, this is the first reported thin single-crystal MHP memristor device and the first time that the electroforming process is recorded through impedance spectroscopy. This device's outstanding stability and performance position it as a promising candidate for high-density data storage and neuromorphic applications.

1. Introduction

MHPs form a new type of semiconductor family that offer energetically favorable fabrication methods and cost-effective performance. MHPs found their first niche application in the field of optoelectronics, becoming a promising candidate for new-generation photovoltaic technology due to their high absorption coefficient, bandgap tunability, and long diffusion lengths.[1–3] These have enabled MHP solar cells to reach power conversion efficiencies (PCE) >25% on a lab scale.[4] Despite this remarkable performance as conventional semiconductors, MHPs also present an intrinsic dual electronic-ionic nature slowing down their response times.[5–7] As a direct result, the presence of hysteresis behavior during current–voltage curves (*jV*) has been a recurring fingerprint for MHPs solar cells, leading to substantial differences in the forward (FS, from short-circuit current density J_{sc} to open-circuit voltageV_{oc}) and reverse scan (RS, from V_{oc} to J_{sc}) performance. This effect provokes a delay between the change of the system properties under variation of an external electric field, leading to resistive changes.[8–10] Along with this ionic influence on the resistance, capacitive effects have also been widely reported in the perovskite literature, using techniques in the frequency domain such as impedance spectroscopy (IS)[11–13] or in the time domain.[14] While effects such as the hysteresis may represent an issue evaluating photovoltaic efficiencies, the ionic conductivity, coupled with the excellent optoelectronic properties of these materials, offer opportunities for novel non-photovoltaic devices such as switchable diodes

I. Fernandez-Guillen, C. A. Aranda, P. F. Betancur, M. Vallés-Pelarda, C. Momblona, T. S. Ripolles, R. Abargues, P. P. Boix
Instituto de Ciencia de los Materiales de la Universidad de Valencia (ICMUV)
Valencia 46980, Spain
E-mail: caranda@uji.es; pablo.p.boix@uv.es

C. A. Aranda
Institute of Advanced Materials (INAM)
University Jaume I
Castellon 12006, Spain

The ORCID identification number(s) for the author(s) of this article can be found under https://doi.org/10.1002/aelm.202300475

DOI: 10.1002/aelm.202300475

C. A. Aranda
Center for Nanoscience and Sustainable Technologies (CNATS)
Department of Physical
Chemical and Natural Systems
Universidad Pablo de Olavide
Seville 41013, Spain

C. Momblona
Instituto de Nanociencia y Materiales de Aragón (INMA)
CSIC-Universidad de Zaragoza
Department of Chemical and Environmental Engineering
Campus Río Ebro-Edificio I+D
Universidad de Zaragoza
C/ Mariano Esquillor S/N, Zaragoza 50018, Spain

C. Momblona
Centro de Investigación Biomédica en Red de Bioingeniería, Biomateriales y Nanomedicina
Instituto de Salud Carlos III
Zaragoza 50018, Spain

Table 1. Overview of different memristor devices based on polycrystal MHPs.

Structure	LRS/HRS	V_{set} [V]	V_{reset} [V]	Endurance [cycles]	Retention [s]	Reference
FTO/$MAPbI_{3-x}Cl_x$/Au	10^4	1.47	−1.41	400	$4.68•10^4$	[36]
FTO/$CsPbBr_3$/Au	10^3	1.5	−1.2	100	10^3	[37]
Ag/$CsPbBr_3$/MoO_3/Ag	100	0.7	−0.8	50	10^4	[38]
ITO/$MAPbI_3$/Au	10	0.7	−0.61	500	10^4	[39]
ITO/PEDOT:PSS/$MAPbBr_3$/Al	$3.6•10^6$	−0.2	3	120	10^4	[40]
PET/ITO/$MAPbI_3$/Au	50	0.7	−0.5	400	10^4	[41]
PET/ITO/$Cs_3Bi_2I_9$/Au	10^3	0.3	−0.5	10^3	10^4	[42]
FTO/c-TiO_2/$MAPbI_{3-x}Cl_x$/Al	$1.9•10^9$	1.10	−1.65	160	$2•10^3$	[28]
ITO/$MAPbI_3$/ZnO/Au	500	0.9	−1.5	100	10^4	[23]
ITO/PEDOT:PSS/$MAPbI_3$/Cu	10^4	−0.6	2	$3•10^3$	$3•10^4$	[43]
Si/SiO_2/Ti/Pt/$MAPbI_3$/Ag	10^6	0.13	−0.13	350	10^4	[44]
PET/ITO/PMMA/$CsPbBr_3$QDs/PMMA/Ag	$6•10^5$	2.6	−2.7	$5•10^3$	$4•10^5$	[45]
Au/$MAPbI_3$/Au	10^8	1.16	0.46	10^3	10^4	[46]

or *memristors*.[15–19] Memristors are devices based on the resistive switching phenomenon governing the hysteresis response: the transition from a high resistance conductance state (HRS) to a low resistance one (LRS) when a specific voltage is applied (ON), that can be restored to the initial state by the application of a specific voltage of the opposite sign (OFF). This switchable internal resistance is the feature allowing to encode information. For applications such as spiking or artificial neural networks, memory elements operating at multiple timescales are required, involving drift (non-volatile) and diffusive (volatile) mechanisms.[20–22] The rich variety of charge dynamics resulting from combining charge carriers and ionic migration, allows MHPs to match with the demanding requirements of a superior memristor device. Non-destructive reading process, high ratio between the current in HRS and LRS state, low voltage operation, high operative times (retention times), high endurance in set/reset (LRS/HRS) cycles operability and fast switching speed, are some of the conditions that seek to meet the latest advances in perovskite-based memory devices.[23–26] Although the MHP-based memristors research shows the potential to present an alternative to conventional oxide industry,[27] there are still many challenges to be solved as endurance and reliability. Most of the work published so far is based on polycrystalline thin film configurations,[28,29] bulk crystals[30,31] halide perovskites, or perovskite nanocrystals.[32] In most of these devices, the unstable response in their steady states limits the access to the working mechanisms. As a result, the exact nature of their working principles is still under debate, and a precise characterization of their electroforming process (the activation of a pristine device to a memristive one) has not been well detailed. In the case of polycrystalline thin films, the challenge is still to obtain high uniformity and smooth surface, due to the solution processing, harming to reach identical electric characteristics for each cell. The presence of grain boundaries and frequent pinholes in polycrystalline thin films, are the origin of parasitic leakage current, favoring degradation pathways that compromise the stability and reliability of perovskite materials as commercial memristors. In addition, the nanometric thickness of polycrystalline films, favors large intrinsic electronic current, which diminishes the ionic migration needed for the memory behavior. To partially overcome these issues, MHP single crystal memristors have been developed. Single crystals can provide considerable ionic transport and low operational current due to the absence of grain boundaries and lower state density of defects. This can be used to design memristive devices with fast switching speed, low energy consumption, and higher endurance. However, the usual thickness of bulk crystals, in a millimetre scale, can also hamper some optoelectronic properties of the material. Optical absorption and emission, charge carrier mobility, surface recombination, and even the mechanical properties of the single crystals, are greatly affected by its elevated thickness.[33–35]

Table 1 shows an overview of different MHP memristive devices. For simple structures (contacts and one buffer layer or less) the devices are characterized by a high LRS/HRS ratio but with high set/reset potentials and low endurance times. There is only one exceptional device with outstanding memristive properties with a simple device architecture, ref 46. Thus, devices with a simple structure need to improve their endurance times by keeping high LRS/LRS ratios. This bottleneck is solved by adding several layers of different materials, such as Pt, Pd, polymethyl methacrylate PMMA, SiO_2, etc. This method improves the endurance time while maintaining a decent LRS/HRS ratio, but manufacturing costs increase significantly, adding the implicit costs of making the devices in glove boxes plus the encapsulation requirement. It should be noted that in this table we have not added the devices whose LRS/HRS ratio is <10.

In this work, we unify the advantages of perovskite polycrystalline thin films with the stability of a single crystal material. We have developed an extremely stable perovskite memristor, with simple architecture and extraordinary endurance by keeping a reasonable LRS/HRS ratio. The device fabrication process is performed under ambient conditions without encapsulation . A wide bandgap perovskite, such as $MAPbBr_3$, is selected to favor the ionic transport in a thin single crystal (TSC) for the memristor device. Exceptional long-time operation is achieved. The current stability reaches 10^4 s with an endurance cycle (set/reset switching) in the order of 10^3. This value, measured under ambient conditions is one of the highest endurance values reported

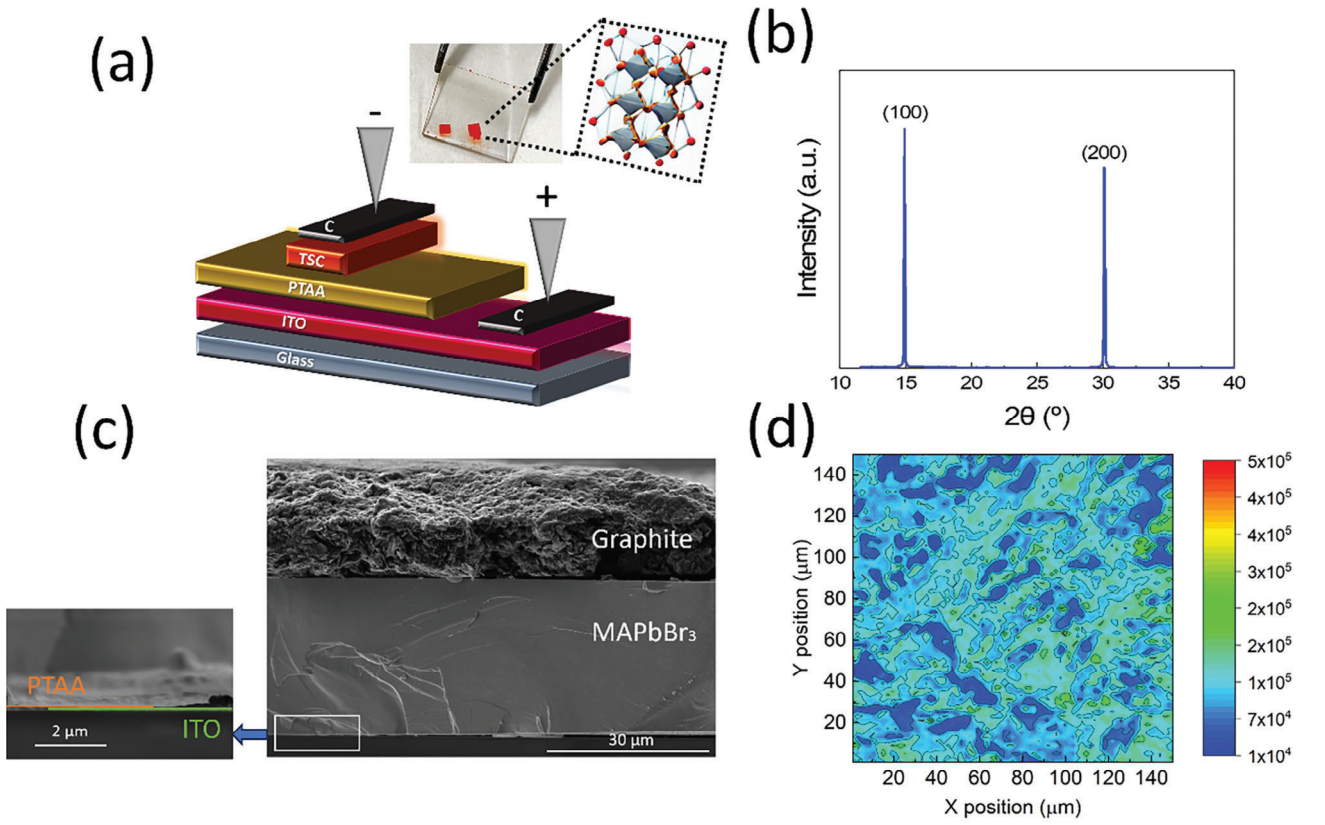

Figure 1. a) Scheme of the complete device for memristor application, using graphite electrodes for the electrical measurements. The inset shows a real photo of the TSC grown onto PTAA layer through ITC confined method. b) X-ray diffraction showing the peaks position corresponding to the cubic phase (100) at 15° and (200) at 30°. c) Cross-section SEM image of one device. d) Photoluminescence mapping of the TSC surface showing high homogeneity.

to date. The stability of the device enables to use impedance spectroscopy (IS) as a tool to unveil the nature of the electroformation process governing the resistive switching. We analyze both the impedance spectra corresponding to the electroforming process and LRS, confirming the role of the ionic motion on the operation mechanism.

2. Results and Discussion

2.1. Crystallization Method and Design of Thin Single Crystal Perovskite Memristor

TSC are monocrystals grown in a confined space where the thickness can be easily controlled, and therefore, their associated properties.[47,48] Thinner crystals are typically more flexible than the thicker ones, able to be bent or stretched without cracking, which is a great advantage for potential flexible memristors. In this confined method, the crystal is grown through a solution of 1.8 M of $PbBr_2$ and MABr in dimethylformamide (DMF): dimethyl sulfoxide (DMSO) 10:1 vol:vol, inserted between two poly (triaryl amine) (PTAA) covered indium tin oxide (ITO) substrates. The sandwiched structure is then heated on a hot plate at room conditions, based on the inverse temperature crystallization (ITC) method (growing method founded on the retrograde solubility behavior of perovskite materials), reaching 60 °C in a ramp of temperature of 15 °C h^{-1}, to precisely control the nucleation and growth of single crystals (see Figure S1, Supporting Information). Reproducible single crystals are achieved with thicknesses between 20 and 30 µm and area of ≈6 mm^2 (see Figure S2, Supporting Information). This micrometre-scale single crystal, instead of nanometer scale polycrystalline thin films, could provide a decreased defect density, reducing thus the surface recombination that could lead to higher charge carrier lifetime than thick single crystals (Figure S3, Supporting Information).[34]

The perovskite composition selected for this work is $MAPbBr_3$. It is chosen due to its intrinsic properties, such as high ions mobility, and both ambient and operational stability, beneficial for memristor application. After the crystallization process, the sandwiched configuration is carefully opened with a blade, resulting on the crystal stacked to just one of the PTAA surfaces. To perform the electronic characterization, a graphite spray was coated on the top of the crystal and on the ITO contact to complete the device (**Figure 1a**). This carbon-based electrode presents several advantages in terms of sustainability, efficiency, cost, and stability, as compared with metal electrodes. The scalability and compatibility with flexible substrates complete the benefits of this selection.[49,50] The electrical measurements were carried out using a customized sample holder specifically designed for this purpose (see Figure S4, Supporting Information).

To study the structural properties of the TSC, X-ray diffraction (XRD) analysis is performed to corroborate its monocrystalline

nature. Sharp and intense XRD reflections along (100) and (200) planes confirm the formation of a highly crystalline perovskite cubic phase (Figure 1b). Representative scanning electron microscopy (SEM) images of the device are shown in Figure 1c. The SEM images confirm thickness of ≈30 μm for the perovskite crystal. Top contact of graphite thickness is ≈15 μm. PTAA, with a thickness of 20 nm, and ITO are shown in the zoom SEM image. To ensure the smoothness of the TSC, we measure photoluminescence mapping to corroborate the homogeneity of surface optical properties of the TSC (Figure 1d). The scanning was performed within an area of 60 μm^2, as a representation of the complete surface of the TSC, between 6 and 7 mm^2.

2.2. Memristor Performance of the Thin Single Crystal Perovskite Device

The structure of a typical resistive switching memristor consists of a top electrode, semiconducting layer and a bottom electrode, forming a two-terminal system. In our case, anode contact is connected in the carbon-based electrode placed on the top of perovskite, meanwhile, cathode is fixed in the carbon electrode deposited on the ITO substrate.

Most of the resistors need a first step known *electroformation*. This process is referred to as the formation of a conducting path that allows the transition from HRS to LRS. Once the conducting path is formed due to the external bias (electroforming process), the device turns into LRS. When the opposite bias is applied, the RESET process occurs due to the breaking of the conducting path, and the HRS is achieved. If the ions do not come back to their original place, the conduction paths built during the electroforming process are just partially broken, and then, after the first RESET, turning the HRS to LRS requires less power. After this, the device stabilizes the voltages set/reset. The mechanism of this process is still under debate due to the difficulties in studying the in situ formation of this abrupt and dynamic process. However, we provide a more in-depth approach to this mechanism with the IS analysis that we propose in below.

After the device has been activated through the electroformation process (see Figure S5, Supporting Information), we perform cyclic voltammetry, applying voltage sweep of 0 V → + 2 V → 0 V → −2.7 V → 0 V to evaluate the initial performance of our memristor device (**Figure 2a**). Along with the charge carrier injection and transport, the applied voltage also redistributes the ionic species or vacancies along the crystal thickness. This ionic movement is key to trigger the different resistive states of the memristor, with a mechanistic origin that is currently under debate and falls beyond the scope of this manuscript (different proposed interpretations include filament formation or interfacial adjustments[51,43] among others[52]). In our case, as the voltage sweeps from 0 to 2 V, a sudden current increase arises at 0.6 V. At this set voltage the device exhibited the transition from HRS to LRS, reaching current values in the order of mA. To fulfill the non-volatile nature of the device, the memristor must maintain its resistance state within a voltage range. To test that, we measure a reverse sweep to negative voltages (from 0 to −2.7 V). At −2.3 V the transition from LRS to HRS occurs, becoming the reset voltage accompanied by a current drop down to the μA range (Figure 2a). To confirm the stability of the device under stressful conditions, 100 *jV* cycles are performed (Figure 2a). Cycles 1, 30, 50, 90, and 100 are displayed with solid color, the rest of the cycles are shown with translucid lines to better overview of the graph. The similarity between the first and last cycle (black line and yellow one, respectively) proves the operational reliability of the device. Figure S6 (Supporting Information) displays 10 jV curves of different devices, probing the reproducibility of the device. Most of the devices show an abrupt transition from LRS to HRS. This transition occurs mainly at −2.3 V after a previous reduction of the reset voltage. This reduction needs three cycles at most to occur, decreasing the voltage from −4 to −2.3 V to finally stabilize. Set voltage is much stable and occurs at 0.6 V in each device.

To compare the cyclic voltammetry performance of our TSC with a polycrystalline device, we fabricated a $MAPbBr_3$ polycrystalline thin film memristor using the same architecture. As seen in Figure S7 (Supporting Information), we evidence the superior LRS/HRS ratio and current values for the monocrystal configuration as compared with the polycrystalline device.

One of the most critical challenges in perovskite memristors is to achieve high endurance by keeping the rest of the outstanding properties with a simple architecture device. Endurance refers to the ability of a memristor to endure or sustain repeated switching cycles without significant degradation or loss of performance. It is particularly important because the repeated switching cycles can introduce various physical phenomena such as electromigration, thermal effects, material fatigue, and degradation of the memristor,[53,54] leading to changes in the memristor's resistance or conductance, resulting in variations in its behavior and potential failure.

Figure 2b, shows the endurance test based on a sequence of voltage steps from +0.1 V → + 1 V → +0.1 V → −2.5 V, where 0.1 V is the reading voltage, 1 V is the set voltage, and −2.5 V acts as reset voltage. The current is measured at 0.1 V alternating the HRS and LRS. First 250 s, HRS lecture increased from 0.1 to 0.3 mA. Subsequently, the current of HRS decreases and the dispersion increases, reaching a current from 0.01 to 0.1 mA. LRS/HRS ratio oscillated from 10 (during the first 250 s) to 80 (for the rest of the measurement). LRS presents high stability of current, keeping the same order of magnitude after 10^3 cycles. Such results are comparable with some perovskite devices with more sophisticated architectures.[55] Figure 2c displays the retention time test, measuring the current in continuous at 0.1 V for both states, first the LRS (blue line) and subsequently, the HRS (orange line) along 10^4 s. HRS current transits from 50 to 80 μA during the first 500 s. Consequently, current is stabilized at 80 μA along the measurement. Meanwhile, the current in the LRS is highly stable along the 10^4 with a LRS/HRS ratio of 25 s, which is another optimal performance indicator of the ReRAM device.[56] Finally, the resistance transition is showed in Figure 2d, evidencing the abrupt change from HRS to LRS at 0.5 V and the reverse transition at −2.0 V. The slope close to the unity is translated into a quick evolution between both states, results expected for memory devices.[57] Additionally, the time response from HRS to LRS transition is shown in Figure S8 (Supporting Information). The time transition is 15 ms. Unfortunately, to the best of our knowledge, time response is not usually reported in MHP memristors and no comparisons can be done.

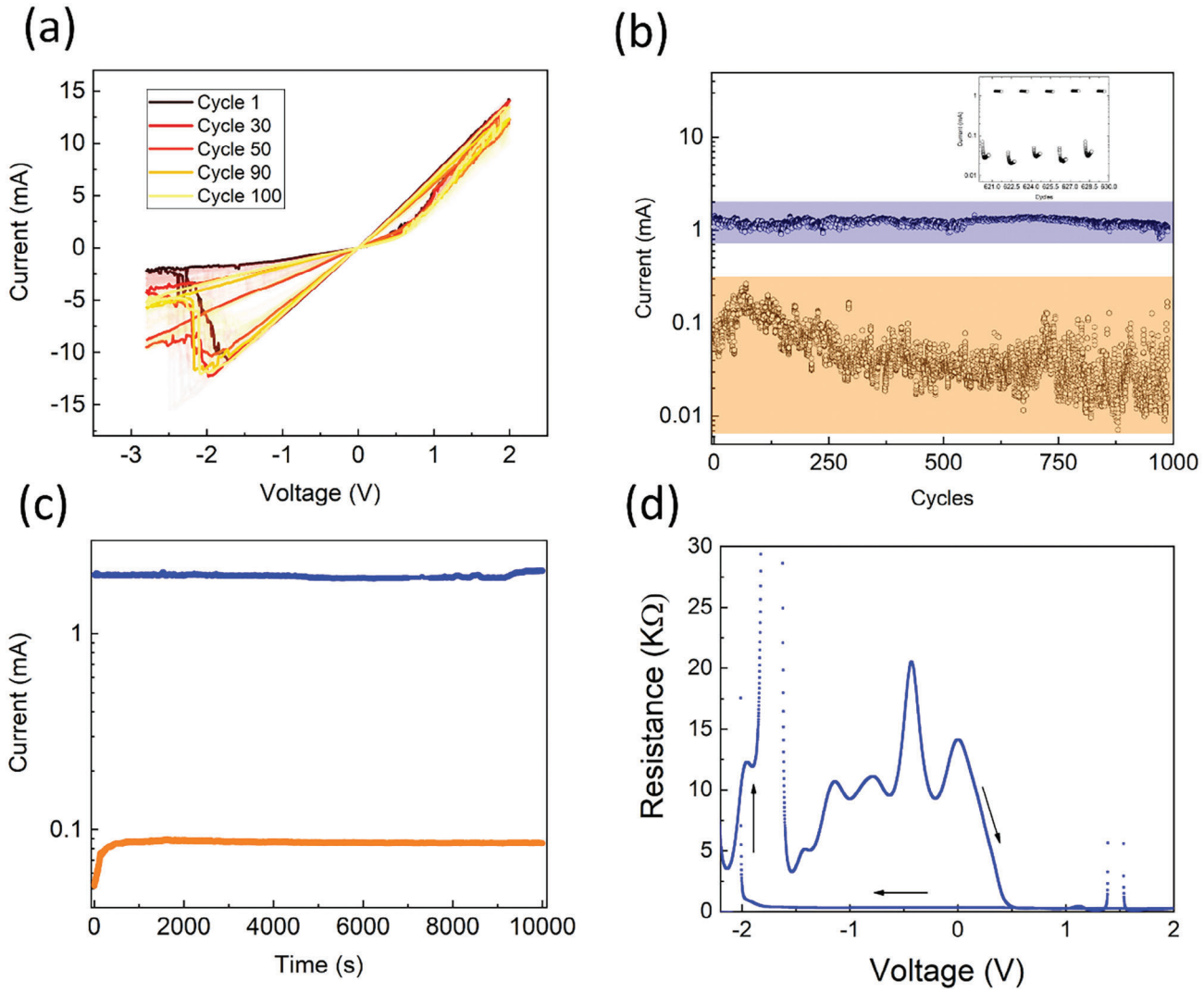

Figure 2. a) Cyclic voltammetry curves in log scale showing SET and RESET processes during 100 cycles at 100 mV s^{-1} of scan rate. b) Endurance performance test upon applying cyclic sweep voltages (+0.1 V → + 1 V → +0.1 V → − 2.5 V → +0.1 V). c) Evolution of current stability performed at LRS (blue line) and HRS (orange line) at 0.1 V of read voltage. d) Resistance measurement during the transition from HRS to LRS and vice versa.

2.3. Impedance Spectroscopy Characterization of the Electroforming Process

As mentioned above, memristors undergo resistive switching via the electroformation process, where the conductive path is established within the perovskite material resulting in the LRS. Understanding this process is key for investigating the factors affecting the switching kinetics, endurance, and variability of perovskite memristors needed for their full potential in computing and memory applications. However, the complex interplay between the ionic and electronic processes operating on different time scales, presents a significant challenge in achieving this goal.[43,58–60] Nevertheless, two different general possibilities can be considered, as reported in literature: i) electrochemical metallization mechanism (ECM) through metal cations, and ii) valence change mechanism (VCM), based on halide vacancies. In halide perovskite-based memristors, the conducting route can involve either metal cations for the ECM or halide vacancies for the VCM.[28,61,62]

IS consists of the electrical measurement of current–voltage of the device at a steady-state potential (V_{dc}) overlapping a small perturbation (V_{ac}) in a range of frequency, ω. The data obtained is reflected in the complex impedance that the device present against that perturbation, depending on the frequency region. The interpretation of these results can be done through fitting to an equivalent circuit. The capacitance in the IS response of metal halide perovskite devices,[63] particularly in the low-frequency range,[64] is linked to the type of current–voltage hysteresis. It can be classified as normal (NH) or inverted (IH). The latter, resulting in higher current in FS than in RS, has been associated with the negative capacitance feature, a distinctive feature also found in neuronal models.[65,66] Consequently, the nature of IS analysis can be of great help in determining the specific processes taking place during the HRS and LRS. IS can be used to analyze

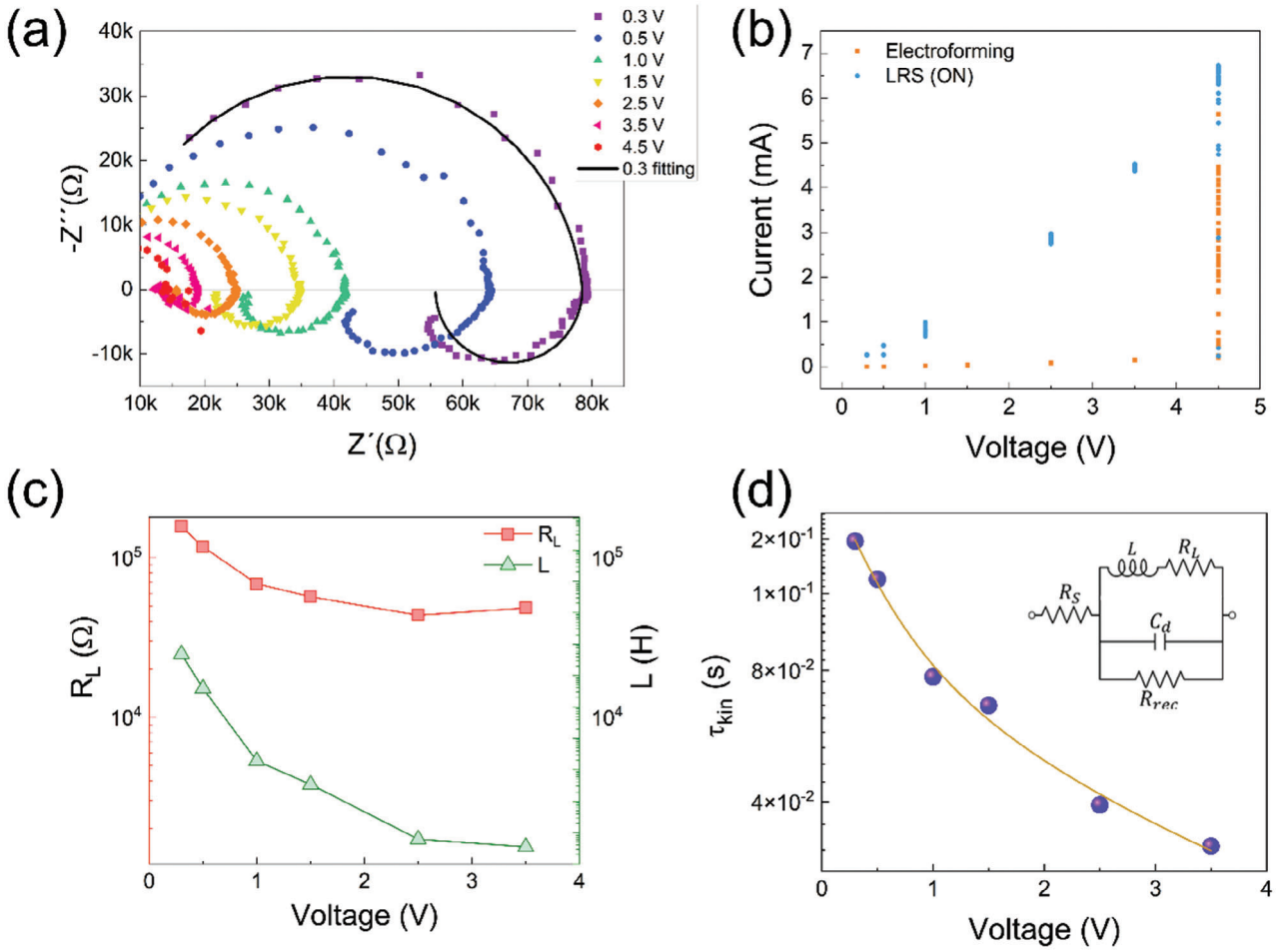

Figure 3. a) Impedance spectra showing the evolution of the response with the applied bias leading to the electroforming process. Fitting is shown just as 0.3 V for clarity. b) DC current corresponding to the electroforming process (orange dots) and LRS (blue dots). c) R_L and L elements quantified through the fitting using the EC (inset Figure 3d) (see Supporting Information). d) Kinetic proper times (τ_{kin}) corresponding to the negative capacitance features present during the electroforming process.

the behavior of the device during the electroforming process by measuring at different V_{dc}, trying to reproduce a current-voltage curve from low applied bias to high applied bias. The pristine device, with no previous treatment, is gradually subjected to rising voltages, from 0 to 4.5 V. All the Nyquist plots present one arc in the high/intermediate frequency (HF, IF) region, which is attributed to bulk processes, and a characteristic loop toward the fourth quadrant at low-frequency domains (LF). This reduction of Im (Z) to values <0 at low frequencies can be observed in different configurations of halide perovskites-based devices, both experimentally and in drift-diffusion simulations.[67,68] It is commonly referred to as "inductive loop" or "negative capacitance"[69] and can be modeled by a chemical inductor parameter.[70,71] It is worth remarking that, in classical semiconductor theory, a conventional electromagnetic induction effect in series would define the shape of the high-frequency part of the spectra. In contrast, the physical origin of this chemical inductor is related to the interplay of charged species (namely charges and ions) moving at different speeds, which can delay the response of the system to the signals and modulate the injected current at the interfaces.[70–72]

A clear evolution of the IS is observed (**Figure 3a**) for each applied V_{dc}: as the voltage increases, both the high-frequency arcs and the inductive behavior become smaller, leading to a quite distorted spectra when reaching 4.5 V. The I_{dc} current produced during the IS is recorded to ensure the stability of the sample during the measure. Figure 3b shows currents of 10^{-6} A at low V_{dc} and how it is increasing linearly up to 10^{-3} A when approximates to 4.5 V. This fact demonstrates that the process of *electroforming* is occurring during the impedance measure (orange points in Figure 3b). The rising up of the current with a change of more than 2 orders of magnitude, together with a change in the impedance spectra, clearly indicates the appearance of a process that leads to an ON state or LRS.

A decrease of the bias applied is then carried out from 4.5 to 0 V. The I_{dc} in this case show how the LRS is maintained, as the I_{dc} still in the mA range at every V_{dc} (blue points in Figure 3b).

The presence of the inductive element leads to a slow time constant τ_{kin} (see Supporting Information for details) that is able to provide enough information about the ionic motion occurring at the LF domain. We proceed then to fit the IS with

the equivalent circuit (EC) (inset Figure 3d) including the R_L-L branch, through which the τ_{kin} is defined. Recently, several publications have confirmed the usefulness of this method in the interpretation of MHP memristors behavior, introducing a general "neuron-style" model that includes a slow time constant that can persist to be nearly independent of the voltage.[71,73,74] The calculated kinetic time decreases with the increased bias, pointing out that the electroforming process is correlated with a change in the time domain that goes from 10^{-1} s to 10^{-2} s when the LRS is reached. Those times can be attributed to ionic accumulation and halide vacancy diffusion, respectively, as previously reported in literature.[75] Therefore, the electroforming process is initiated by an accumulation of ions, that gradually evolves to the stages determined by the faster processes of ion diffusion. A similar sequence has already been reported recently for memristors based on metal oxides, so we could suggest a similar basis of mechanisms, as demonstrated by IS.[76] This finding confirms the ionic role on the memristor mechanism, and marks the first time that the electroforming process is recorded in situ through IS.

3. Conclusion

We have successfully fabricated the first thin single-crystal perovskite memristor, which combines the advantageous properties of monocrystalline materials and thin-film perovskites. Through the confined inverse temperature crystallization (ITC) method, using ITO and PTAA as bottom electrodes and a graphite spray as a metal contact, we achieved a highly stable device with exceptional performance. Our memristor exhibited a remarkable ON/OFF ratio of 10 and endurance of 10^3 cycles, representing one of the highest reported values in literature. The device's stability under ambient conditions, without the need for encapsulation, allowed us to perform a comprehensive impedance analysis. Notably, we successfully recorded the electroforming process in situ, shedding light on the mechanism governing perovskite memristor operation.

By quantifying the gradual kinetic changes (τ_{kin}) related to the low-frequency response, we uncovered the modification of ionic motion during the electroforming process that leads to a three-order magnitude variation in the current response. The calculated kinetic changes show a decreasing trend: the electroforming goes from long times to shorter times, that could be related to different ion dynamics (from accumulation to diffusion).

These findings significantly contribute to our understanding of perovskite memristor behavior. Moreover, our fabrication approach offers a simple and efficient method for producing efficient and reliable perovskite memristors.

Overall, this work represents a significant step forward in advancing perovskite memristor technology, opening new possibilities for high-performance and stable devices for future applications.

4. Experimental Section

Materials: Lead bromide ($PbBr_2$) was purchased from TCI. Methylammonium bromide (CH_3NH_3Br) was purchased from GreatCell. Polytriarylamine (PTAA) was purchased from Ossila. N,N-dimethylformamide (DMF) and Dimethyl sulfoxide (DMSO) were purchased from Thermo Scientific. Toluene was purchased from VWR. Graphite spray was purchased from RS. All the reagents were directly used without any further purification.

Fabrication Process: Monocrystal devices: The $MAPbBr_3$ precursor solution of 1.8 M was prepared by dissolving 1:1 molar ratio of $PbBr_2$ and CH_3NH_3Br in 10:1 ratio of DMF:DMSO in a vial with vigorous shaking. PTAA was dissolved in toluene with 2 mg mL^{-1}. All the solution were filtrated using 0.2 µm PTFE syringe filter before deposition. Glass/ITO substrates were cleaned by acetone, detergent, deionized water, and absolute ethanol in an ultrasonic bath for 10 min for each step. After drying with a high air flow, the substrates were treated in a UV ozone cleaner for 20 min. Subsequently, 60 µL of the prepared PTAA solution was deposited onto the ITO substrate by spin-coater at 4000 rpm for 30 s under room conditions. Immediately, the substrates were annealed at 100 °C for 10 min. Therefore, 40 µL of the $MAPbBr_3$ solution were dropped on the as-prepared substrate and enclosed by another PTAA-coated substrate. The space-confined inverse temperature crystallization method was used for growing thin single crystals.[77] The temperature was increased from 25 to 60 °C with a ramp of 15 °C h^{-1}. The substrates were held at 60 °C for 48 h. After cooling at room temperature, the substrates were separated with a blade. Finally, the graphite electrodes were added on the $MAPbBr_3$ and ITO by deposing 10 µL of the solution with a micropipette. The solution evaporates in ≈60 s after deposition, forming a solid graphite that acts as an electrode. It is important to underline that the device is fabricated out of glovebox.

Polycrystal Devices: A solution of 1.4 M of $MAPbBr_3$ dissolved in DMF:DMSO (1:4, vol:vol) was added on the ITO substrates treated with PTAA, as previously described. Subsequently, the solution was spinning with a ramp of 1000 rpm for 10 s and 4000 rpm for 40 s, adding 1 mL of toluene at 12 s of the second ramp. Then, the device is annealed for 30 min. Finally, the graphite electrodes were deposited on the $MAPbBr_3$ and ITO. All the device process was fabricated in glovebox.

Characterization: The crystalline structure was assessed by a XRD collected on a Bruker D8 Advanced X-ray diffractometer with copper Ka radiation (l = 1.5418 A°) and at a scan rate of 5 ° min^{-1} for 2θ angles ranging from 12 to 40. Scanning electron microscope (SEM) images were captured by an S-4800 instrument from HITACHI (Tokyo, Japan) operating at 2 kV. Photoluminescence spectra was done using a confocal microphotoluminescence (micro-PL) spectroscopy system, with the samples placed in the cold finger of a vibration-free closed-cycle cryostat (AttoDRY800 from Attocube AG). Excitation and detection were carried out using a 50X microscope objective with a long working distance and a numerical aperture of NA = 0.42, which was placed outside the cryostat. The sample's emission was long-pass filtered, dispersed by a double 0.3 m focal length grating spectrograph (Acton SP-300i from Princeton Instruments), and detected with a cooled Si CCD camera (Newton EMCCD from ANDOR) for recording micro-PL spectra, and a silicon single-photon avalanche photodiode detector (from Micro Photon Devices) connected to a time-correlated single-photon counting electronic board (TCC900 from Edinburgh Instruments) for micro-TRPL measurements. Impedance spectroscopy (IS) and electrical characterization were measured using a Gamry interface 1010E.

Supporting Information

Supporting Information is available from the Wiley Online Library or from the author.

Acknowledgements

C.A.A was supported by the Margarita Salas postdoctoral contract MGS/2021/24(UP2021-021) financed by the European Union-NextGenerationEU. The authors would like to acknowledge the funding by MCIN/ AEI /10.13039/501100011033 (Research project no. PID2020-119628RB-C31). PPB and TR thank Generalitat Valenciana for the funding via Pla Gent-T (grants CIDEXG/2022/34). C.M. acknowledges the funding from the "Contratación de personal investigador doctor con experiencia internacional CDEIGENT" (ref CDEIGENT/2021/2022) from the Consellería de Innovación, Universidades, Ciencia y Sociedad Digital de la Generalitat Valenciana, Spain.This study forms part of the Advanced Materials programme and was supported by MCIN with funding from European Union NextGenerationEU (PRTR-C17.I1) and by the Generalitat Valenciana (code MFA/2022/040 /007). The work was partially funded by MCIN/ AEI through project TED2021-131600B-C32.

Conflict of Interest

The authors declare no conflict of interest.

Data Availability Statement

The data that support the findings of this study are available from the corresponding author upon reasonable request.

Keywords

electroforming, endurance, impedance spectroscopy, memristors, perovskite

Received: July 15, 2023
Revised: November 24, 2023
Published online:

[1] M. A. Green, A. Ho-Baillie, H. J. Snaith, *Nat. Photonics* **2014**, *8*, 506.
[2] H. S. Jung, N.-G. Park, *Small* **2015**, *11*, 10.
[3] J.-P. Correa-Baena, M. Saliba, T. Buonassisi, M. Grätzel, A. Abate, W. Tress, A. Hagfeldt, *Science* **2017**, *358*, 739.
[4] H. Min, D. Y. Lee, J. Kim, G. Kim, K. S. Lee, J. Kim, M. J. Paik, Y. K. Kim, K. S. Kim, M. G. Kim, T. J. Shin, S. Il Seok, *Nature* **2021**, *598*, 444.
[5] W. Tress, *J. Phys. Chem. Lett.* **2017**, *8*, 3106.
[6] P. Calado, A. M. Telford, D. Bryant, X. Li, J. Nelson, B. C. O'regan, P. R. F. Barnes, *Nat. Commun.* **2016**, *7*, 13831.
[7] P. Lopez-Varo, J. A. Jiménez-Tejada, M. García-Rosell, J. A. Anta, S. Ravishankar, A. Bou, J. Bisquert, *ACS Energy Lett.* **2017**, *2*, 1450.
[8] D. A. Jacobs, Y. Wu, H. Shen, C. Barugkin, F. J. Beck, T. P. White, K. Weber, K. R. Catchpole, *Phys. Chem. Chem. Phys.* **2017**, *19*, 3094.
[9] Y. Rong, Y. Hu, S. Ravishankar, H. Liu, X. Hou, Y. Sheng, A. Mei, Q. Wang, D. Li, M. Xu, J. Bisquert, H. Han, *Energy Environ. Sci.* **2017**, *10*, 2383.
[10] S. Ravishankar, S. Gharibzadeh, C. Roldán-Carmona, G. Grancini, Y. Lee, M. Ralaiarisoa, A. M. Asiri, N. Koch, J. Bisquert, M. K. Nazeeruddin, *Joule* **2018**, *2*, 788.
[11] O. Almora, I. Zarazua, E. Mas-Marza, I. Mora-Sero, J. Bisquert, G. Garcia-Belmonte, *J. Phys. Chem. Lett.* **2015**, *6*, 1645.
[12] P. Lopez-Varo, J. A. Jiménez-Tejada, M. García-Rosell, S. Ravishankar, G. Garcia-Belmonte, J. Bisquert, O. Almora, *Adv. Energy Mater.* **2018**, *8*, 1702772.
[13] I. Zarazua, J. Bisquert, G. Garcia-Belmonte, *J. Phys. Chem. Lett.* **2016**, *7*, 525.
[14] D. Kumbhar, M. Jain, A. Solanki, *2022 Int. Conf. Adv. Technol. ICONAT*, **2022**, https://doi.org/10.1109/ICONAT53423.2022.9725938.
[15] K. Sakhatskyi, R. A. John, A. Guerrero, S. Tsarev, S. Sabisch, T. Das, G. J. Matt, S. Yakunin, I. Cherniukh, M. Kotyrba, Y. Berezovska, M. I. Bodnarchuk, S. Chakraborty, J. Bisquert, M. V. Kovalenko, *ACS Energy Lett.* **2022**, *7*, 3401.
[16] X. Zhao, H. Xu, Z. Wang, Y. Lin, Y. Liu, *InfoMat* **2019**, *1*, 183.
[17] F. Haque, M. Mativenga, *Jpn. J. Appl. Phys.* **2020**, *59*, 081002.
[18] X. Yan, X. Han, Z. Fang, Z. Zhao, Z. Zhang, J. Sun, Y. Shao, Y. Zhang, L. Wang, S. Sun, Z. Guo, X. Jia, Y. Zhang, Z. Guan, T. Shi, *Front. Phys.* **2023**, *18*, 63301.
[19] Parveen, S., Manamel, L. T., Mukherjee, A., Sagar, S., Das, B. C., *Adv. Mater. Interfaces* **2022**, *9*, 2200562.
[20] Z. Wang, S. Joshi, S. E. Savel'ev, H. Jiang, R. Midya, P. Lin, M. Hu, N. Ge, J. P. Strachan, Z. Li, Q. Wu, M. Barnell, G.-L. Li, H. L. Xin, R. S. Williams, Q. Xia, J. J. Yang, *Nat. Mater.* **2017**, *16*, 101.
[21] E. J. Fuller, S. T. Keene, A. Melianas, Z. Wang, S. Agarwal, Y. Li, Y. Tuchman, C. D. James, M. J. Marinella, J. J. Yang, A. Salleo, A. A. Talin, *Science* **2019**, *364*, 570.
[22] G. Karunaratne, M. Le Gallo, G. Cherubini, L. Benini, A. Rahimi, A. Sebastian, *Nat. Electron.* **2020**, *3*, 327.
[23] B. Hwang, J.-S. Lee, *Sci. Rep.* **2017**, *7*, 673.
[24] H. Kim, M.-J. Choi, J. M. Suh, J. S. Han, S. G. Kim, Q. V. Le, S. Y. Kim, H. W. Jang, *NPG Asia Mater* **2020**, *12*, 21.
[25] M.-C. Yen, C.-J. Lee, K.-H. Liu, Y. Peng, J. Leng, T.-H. Chang, C.-C. Chang, K. Tamada, Y.-J. Lee, *Nat. Commun.* **2021**, *12*, 4460.
[26] H. Kim, J. S. Han, S. G. Kim, S. Y. Kim, H. W. Jang, *J. Mater. Chem. C* **2019**, *7*, 5226.
[27] D.-H. Kwon, K. M. Kim, J. H. Jang, J. M. Jeon, M. H. Lee, G. H. Kim, X.-S. Li, G.-S. Park, B. Lee, S. Han, M. Kim, C. S. Hwang, *Nat. Nanotechnol.* **2010**, *5*, 148.
[28] K. Yan, M. Peng, X. Yu, X. Cai, S. Chen, H. Hu, B. Chen, X. Gao, B. Dong, D. Zou, *J. Mater. Chem. C* **2016**, *4*, 1375.
[29] E. Yoo, M. Lyu, J.-H. Yun, C. Kang, Y. Choi, L. Wang, *J. Mater. Chem. C* **2016**, *4*, 7824.
[30] J. Xing, C. Zhao, Y. Zou, W. Kong, Z. Yu, Y. Shan, Q. Dong, D. Zhou, W. Yu, C. Guo, *Light: Sci. Appl.* **2020**, *9*, 111.
[31] J. Cui, X. Fu, H. Zhou, J. Yin, M. Wu, X. Zhang, *Dalton Trans.* **2021**, *50*, 10365.
[32] R. A. John, Y. Demirag, Y. Shynkarenko, Y. Berezovska, N. Ohannessian, M. Payvand, P. Zeng, M. I. Bodnarchuk, F. Krumeich, G. Kara, I. Shorubalko, M. V. Nair, G. A. Cooke, T. Lippert, G. Indiveri, M. V. Kovalenko, *Nat. Commun.* **2022**, *13*, 2074.
[33] H.-H. Fang, J. Yang, S. Adjokatse, E. Tekelenburg, M. E. Kamminga, H. Duim, J. Ye, G. R. Blake, J. Even, M. A. Loi, *Adv. Funct. Mater.* **2020**, *30*, 1907979.
[34] X. Chen, H. Lu, Z. Li, Y. Zhai, P. F. Ndione, J. J. Berry, K. Zhu, Y. Yang, M. C. Beard, *ACS Energy Lett.* **2018**, *3*, 2273.
[35] Y. Yuan, M. Chen, S. Yang, X. Shen, Y. Liu, D. Cao, *J. Lumin.* **2020**, *226*, 117471.
[36] F. Zhou, Y. Liu, X. Shen, M. Wang, F. Yuan, Y. Chai, *Adv. Funct. Mater.* **2018**, *28*, 1800080.
[37] H. Cai, G. Ma, Y. He, L. Lu, J. Zhang, H. Wang, *Ceram. Int.* **2019**, *45*, 1150.
[38] C. Zou, L. He, L. Y. Lin, *Phys. Status Solidi RRL* **2019**, *13*, 1900182.
[39] J. H. Heo, D. H. Shin, S. H. Moon, M. H. Lee, D. H. Kim, S. H. Oh, W. Jo, S. H. Im, *Sci. Rep.* **2017**, *7*, 16586.

[40] Y. H. Lee, D. H. Kim, C. Wu, T. W. Kim, *Org. Electron.* **2018**, *62*, 412.
[41] C. Gu, J.-S. Lee, *ACS Nano* **2016**, *10*, 5413.
[42] B.-M. Bresolin, C. Günnemann, D. W. Bahnemann, M. Sillanpää, *Nanomaterials* **2020**, *10*, 763.
[43] G. Lin, Y. Lin, R. Cui, H. Huang, X. Guo, C. Li, J. Dong, X. Guo, B. Sun, *J. Mater. Chem. C* **2015**, *3*, 10793.
[44] J. Choi, S. Park, J. Lee, K. Hong, D.-H. Kim, C. W. Moon, G. D. Park, J. Suh, J. Hwang, S. Y. Kim, H. S. Jung, N.-G. Park, S. Han, K. T. Nam, H. W. Jang, *Adv. Mater.* **2016**, *28*, 6562.
[45] L. Jiao, Y. Wang, H.-L. Jiang, Q. Xu, *Adv. Mater.* **2018**, *30*, 1703663.
[46] K. T. Kang, J. Park, D. Suh, W. S. Choi, *Adv. Mater.* **2019**, *31*, 1803732.
[47] L. Lee, J. Baek, K. S. Park, Y.-E. Lee, N. K. Shrestha, M. M. Sung, *Nat. Commun.* **2017**, *8*, 15882.
[48] Y.-X. Chen, Q.-Q. Ge, Y. Shi, J. Liu, D.-J. Xue, J.-Y. Ma, J. Ding, H.-J. Yan, J.-S. Hu, L.-J. Wan, *J. Am. Chem. Soc.* **2016**, *138*, 16196.
[49] D. Bogachuk, B. Yang, J. Suo, D. Martineau, A. Verma, S. Narbey, M. Anaya, K. Frohna, T. Doherty, D. Müller, J. P. Herterich, S. Zouhair, A. Hagfeldt, S. D. Stranks, U. Würfel, A. Hinsch, L. Wagner, *Adv. Energy Mater.* **2022**, *12*, 2103128.
[50] D. Bogachuk, S. Zouhair, K. Wojciechowski, B. Yang, V. Babu, L. Wagner, B. Xu, J. Lim, S. Mastroianni, H. Pettersson, A. Hagfeldt, A. Hinsch, *Energy Environ. Sci.* **2020**, *13*, 3880.
[51] P. C. Harikesh, B. Febriansyah, R. A. John, N. Mathews, *MRS Bull. 45*, 641.
[52] X. Xiao, J. Hu, S. Tang, K. Yan, B. Gao, H. Chen, D. Zou, *Adv. Mater. Technol.* **2020**, *5*, 1900914.
[53] K. M. Kim, S. E. Lee, J. Yoon, J. H. Heo, C. Choi, Y. Park, *Sci. Rep.* **2016**, *6*, 36815.
[54] D. Sanjay Khone, S. Bera, A. Singh Rana, *Mater. Today Proc.* **2023**, *3*, https://doi.org/10.1016/j.matpr.2023.03.238.
[55] S. G. Kim, Q. Van Le, J. S. Han, H. Kim, M.-J. Choi, S. A. Lee, T. L. Kim, S. B. Kim, S. Y. Kim, H. W. Jang, *Adv. Funct. Mater.* **2019**, *29*, 1906686.
[56] J. J. Yang, D. B. Strukov, D. R. Stewart, *Nat. Nanotechnol.* **2013**, *8*, 13.
[57] Y. Rong, Y. Hu, A. Mei, H. Tan, M. I. Saidaminov, S. I. Seok, M. D. McGehee, E. H. Sargent, H. Han, *Science* **2018**, *361*, eaat8235.
[58] D. J. Kim, Y. J. Tak, W.-G. Kim, J. K. Kim, J. H. Kim, H. J. Kim, *Adv. Mater. Interfaces* **2017**, *4*, 1601035.
[59] X. Guan, W. Hu, M. A. Haque, N. Wei, Z. Liu, A. Chen, T. Wu, *Adv. Funct. Mater.* **2018**, *28*, 1704665.
[60] X. Zhu, W. D. Lu, *ACS Nano* **2018**, *12*, 1242.
[61] B. Hwang, C. Gu, D. Lee, J.-S. Lee, *Sci. Rep.* **2017**, *7*, 43794.
[62] K. Sun, Q. Wang, L. Zhou, J. Wang, J. Chang, R. Guo, B. K. Tay, X. Yan, *Sci. China Mater.* **2023**, *66*, 2013.
[63] O. Almora, K. T. Cho, S. Aghazada, I. Zimmermann, G. J. Matt, C. J. Brabec, M. K. Nazeeruddin, G. Garcia-Belmonte, *Nano Energy* **2018**, *48*, 63.
[64] S.-M. Yoo, S. J. Yoon, J. A. Anta, H. J. Lee, P. P. Boix, I. Mora-Seró, *Joule* **2019**, *3*, 2535.
[65] A. O. Alvarez, R. Arcas, C. A. Aranda, L. Bethencourt, E. Mas-Marzá, M. Saliba, F. Fabregat-Santiago, *J. Phys. Chem. Lett.* **2020**, *11*, 8417.
[66] C. Gonzales, A. Guerrero, J. Bisquert, *J. Phys. Chem. C* **2022**, *126*, 13560.
[67] F. Ebadi, N. Taghavinia, R. Mohammadpour, A. Hagfeldt, W. Tress, *Nat. Commun.* **2019**, *10*, 1574.
[68] D. A. Jacobs, H. Shen, F. Pfeffer, J. Peng, T. P. White, F. J. Beck, K. R. Catchpole, *J. Appl. Phys.* **2018**, *124*, 225702.
[69] D. Klotz, *Electrochem. Commun.* **2019**, *98*, 58.
[70] J. Bisquert, A. Guerrero, *J. Am. Chem. Soc.* **2022**, *144*, 5996.
[71] E. Hernández-Balaguera, J. Bisquert, *ACS Energy Lett.* **2022**, *7*, 2602.
[72] S. Ravishankar, O. Almora, C. Echeverría-Arrondo, E. Ghahremanirad, C. Aranda, A. Guerrero, F. Fabregat-Santiago, A. Zaban, G. Garcia-Belmonte, J. Bisquert, *J. Phys. Chem. Lett.* **2017**, *8*, 915.
[73] M. Berruet, J. C. Pérez-Martínez, B. Romero, C. Gonzales, A. M. Al-Mayouf, A. Guerrero, J. Bisquert, *ACS Energy Lett.* **2022**, *7*, 1214.
[74] J. Bisquert, *J. Phys. Chem. Lett.* **2023**, *14*, 1014.
[75] H. Wang, A. Guerrero, A. Bou, A. M. Al-Mayouf, J. Bisquert, *Energy Environ. Sci.* **2019**, *12*, 2054.
[76] G. Zhou, X. Ji, J. Li, F. Zhou, Z. Dong, B. Yan, B. Sun, W. Wang, X. Hu, Q. Song, L. Wang, S. Duan, *iScience* **2022**, *25*, 105240.
[77] R. K. Battula, G. Veerappan, P. Bhyrappa, C. Sudakar, E. Ramasamy, *Surf. Interfaces* **2023**, *36*, 102475.